CONVECTIVE TRANSPORT OF TRACE SPECIES OBSERVED DURING THE STRATOSPHERE–TROPOSPHERE ANALYSES OF REGIONAL TRANSPORT 2008 EXPERIMENT (START08)

A Thesis

by

LEONG WAI SIU

Submitted to the Office of Graduate and Professional Studies of
Texas A&M University
in partial fulfillment of the requirements for the degree of

MASTER OF SCIENCE

Chair of Committee,	Kenneth P. Bowman
Committee Members,	Craig C. Epifanio
	Shari A. Yvon-Lewis
Head of Department,	Ping Yang

December 2014

Major Subject: Atmospheric Sciences

Copyright 2014 Leong Wai Siu

ABSTRACT

During the Stratosphere–Troposphere Analyses of Regional Transport 2008 Experiment (START08) the NCAR/NSF Gulfstream V aircraft encountered high concentrations of NO and NO_y in the upper troposphere downwind of a squall line in north Texas, suggesting either convective transport of polluted boundary layer air to the upper troposphere or lightning induced production of nitrogen oxides in the convection. These hypotheses are tested by computing three-dimensional back-trajectories using winds from a high-resolution simulation of the event with the Weather Research and Forecasting (WRF) Model. The WRF model simulation reproduces the storm structure and evolution with good fidelity. The back trajectories reveal two distinct layers of outflow air from different mesoscale convective systems (MCSs). Most air in the upper layer is transported northward from an MCS in south Texas, while the lower layer is from both the squall line and the southern MCS. The predicted concentrations of CO and NO_y using a simple chemical model show that the back trajectories capture the vertical profile of CO in the lower layer and of NO_y at the bottom and top of the lower layer. The enhanced NO_y could be explained by lightning during the time the outflow air was ascending in the convective updrafts using data from the National Lightning Detection Network (NLDN). In the upper layer, the large discrepancy of NO_y between observation and model seems to be caused by the lack of lightning source and a notable underestimate of the vertical transport to the very top of the troposphere by the MCS.

DEDICATION

To my Chinese Language and Culture teacher, Wai Ting Leung (1945–2012)

ACKNOWLEDGEMENTS

First, I would like to express my deepest gratitude to my advisor, Kenneth Bowman. I am also indebted to my thesis committee members, Craig Epifanio and Shari Yvon-Lewis, for providing constructive comments on the thesis. Then I would like to thank Richard Orville and Gary Huffines for providing the lightning data and assistance with using the data, Craig Epifanio for running the WRF model, and Cameron Homeyer for processing the NEXRAD Level II data. Appreciation must also go to my group mates David Solomon and John Cooney. This research is funded by National Science Foundation grant AGS-1016191 to Texas A&M University.

TABLE OF CONTENTS

Page

LIST OF FIGURES

FIGURE Page

LIST OF TABLES

TABLE Page

1. INTRODUCTION

Each year around 100,000 thunderstorms take place in the United States (U.S.) (*Jaeglé*, 2007). Convective transport by thunderstorms has long been known to have an important influence on the chemical composition of the upper troposphere (UT) (e.g., *Dickerson et al.*, 1987; *Pickering et al.*, 1990; *Poulida et al.*, 1996; *Ridley et al.*, 2004a; *Bertram et al.*, 2007). In a convective system, the characteristic vertical velocity of updraft cores can be more than 15 m s^{-1} (*Dye et al.*, 2000), which gives a vertical transport time through the depth of the troposphere of less than an hour (*Bertram et al.*, 2007). Compared with the BL, reaction rates, except photolysis, are usually reduced in the rather cold and dry UT. The result is that, once lofted to the UT, many trace gases have chemical lifetimes that are longer than the convective transport time. Also, while the typical size of a convective system is of the order of 100 km, trace gases in the UT can be carried by upper-level winds around globe and can stay near the UT for more than a week (*Stenchikov et al.*, 1996; *Ridley et al.*, 2004a). Deep convection impacts the global climate in two principal ways. First, ozone (O_3) and aerosols are produced by chemical reactions of trace gases in the UT. Second, water vapor (H_2O) is transported from the moist lower troposphere (LT) to the UT, where it is the major greenhouse gas (*Lacis et al.*, 1990; *Jaeglé*, 2007).

Tropospheric chemistry plays an important role in both the production and destruction of tropospheric ozone (*Liu et al.*, 1980). Ozone precursors, particularly NO_x ($NO + NO_2$), hydrocarbons, and carbon monoxide (CO), are responsible for producing O_3 through a series of photochemical reactions (*Bradshaw et al.*, 2000). For example, NO_x acts as a catalyst in producing O_3 during the oxidation of CO to

carbon dioxide (CO_2). The lifetime of NO_x extends from about 1 to 2 days in the BL to 2 weeks in the UT, but it is still much shorter than CO, which has a lifetime of a few months (*Seinfeld and Pandis*, 2006). The amount of NO_x is low in the troposphere because it is very reactive (*Logan*, 1983). This makes NO_x a rate-determining tracer in the above processes (*Lelieveld and Crutzen*, 1994; *Crutzen and Lelieveld*, 2001). Using a one-dimensional photochemical model, *Pickering et al.* (1990) show that ozone precursors at the earth's surface can enhance the production of upper tropospheric ozone fourfold.

It is important to determine the distribution of NO_x in the troposphere and its production and removal mechanisms. The major sources of NO_x in the BL include fossil fuel combustion, biomass burning, and emissions from the soil or oceans, whereas stratospheric intrusions, lightning, and aircraft emissions contribute the most to NO_x in the free troposphere (*Bradshaw et al.*, 2000; *Crutzen and Lelieveld*, 2001). The production of NO from lightning is particularly important because it is associated with deep convection in thunderstorms. The distribution of tropospheric NO_x, however, remains highly uncertain. For example, NO_x emission from lightning has been estimated to be between 2 and 20 Tg N yr^{-1}, which means it could be either a small source or a major contributor to tropospheric NO_x (*DeCaria et al.*, 2000; *Schumann and Huntrieser*, 2007).

Many observational and modeling studies have been devoted to examining the influence of convective transport by mid-latitude thunderstorms, especially in the anvil region (e.g., *Dickerson et al.*, 1987; *Skamarock et al.*, 2000; *Ridley et al.*, 2004b). Large-scale models typically parameterize convective transport. With sufficient resolution, mesoscale models can explicitly simulate convection, but they still rely on parameterizations of microphysical processes, sub-grid-scale transport processes, and atmospheric radiation. *Barth et al.* (2007) show that high-resolution mesoscale mod-

els are able to reproduce observed storm structure and kinematics in specific simulations. Air parcel trajectories can help to understand transport pathways and determine the origin of selected air masses. *Jaeglé et al.* (1997) justify the underestimation of hydroperoxyl (HO_2) in the model by injecting methyl hydroperoxide (CH_3OOH) and formaldehyde (CH_2O) and computing their isentropic trajectories. *Skamarock et al.* (2000) demonstrate from trajectory analysis that the anvil air in a simulated multicellular convective system rose up from a layer between 0.5 and 2 km above the surface.

The main objective of this study is to determine the origins and transport pathways of air in the outflow region of a squall line system observed during the Stratosphere–Troposphere Analyses of Regional Transport 2008 (START08) field campaign. Trace gas measurements from the aircraft show two distinct outflow layers ahead of the squall line. It is hypothesized that these outflows are transported from the BL to the upper troposphere by the squall line. To test this hypothesis, the squall line system is simulated with a three-dimensional (3-D) convection-permitting model. The model produces a good simulation of the squall line in terms of the vertical and horizontal structures of the storm. We use multiple *in situ* trace gas measurements from START08 and data from the National Lightning Detection Network (NLDN) to deduce the sources of NO and total reactive nitrogen [$NO_y = NO_x$ + all compounds from the oxidation of NO_x] observed in the outflow air.

2. DATA AND METHODS

2.1 Aircraft Observations

From April to June of 2008, the START08 field campaign used the National Science Foundation/National Center for Atmospheric Research (NSF/NCAR) Gulfstream-V (GV) aircraft to study the chemical and dynamical characteristics of the mid-latitude upper troposphere and lower stratosphere (UTLS) region (*Pan et al.*, 2010). Eighteen research flights (RF01–RF18) with a total of 123 flight hours extensively covered central North America and the Gulf of Mexico between ∼25°–65°N and ∼120°–85°W. The standard instruments on the aircraft measured state parameters such as position, altitude, ambient air temperature, and humidity. The aircraft was also equipped with instruments to measure atmospheric trace gases and microphysical parameters.

In this study, trace gas observations from Research Flight 8 (RF08), including O_3, CO, NO, NO_y, and H_2O, are analyzed. Ozone is measured by a dual-beam ultraviolet absorption ozone photometer. In general the lowest detection limit of O_3 concentration is 1.5×10^{10} molecules cm^{-3} (one-sigma) and the maximum uncertainty at 22 km is 3.6% (*Proffitt and McLaughlin*, 1983). Carbon monoxide is measured by a vacuum-ultraviolet resonance fluorescence (VURF) instrument. The precision of the instrument is ±1.5 ppbv at an ambient mixing ratio of 100 ppbv CO and the uncertainty is 2.4% (*Gerbig et al.*, 1999). The data collected during this campaign are consistent with the measurements from the Harvard University Quantum Cascade Laser System (QCLS) (*Kosterev et al.*, 2002). Nitric oxide and total reactive nitrogen are measured by a 2-channel instrument. Nitric oxide chemiluminescence is detected when NO reacts with O_3 to produce excited nitrogen dioxide (NO_2) (*Ridley*

et al., 2004b). Total reactive nitrogen is detected as a result of the reduction of NO_y with CO. The precision of 1-second data is about 5–10 pptv. The uncertainty of the detector is estimated to be 10%, which improves for large mixing ratios (>50 pptv). Water vapor is measured by the Vertical Cavity Surface Emitting Laser (VCSEL) hygrometer (*Zondlo et al.*, 2010). The instrument measures the absolute concentration of water vapor (molecules cm^{-3}) and is designed for both the troposphere and lower stratosphere (LS). The accuracy of the hygrometer is 10% and the precision is better than 1% in most situations. All of the above instruments provide data at 1 Hz.

2.2 Radar Data

Radar data, which are archived at the National Climatic Data Center (NCDC), are from the Next Generation Weather Radar (NEXRAD) system. This program collects data from the Weather Surveillance Radar–1988 Doppler (WSR-88D) network (*Crum et al.*, 1993). This study uses Level II reflectivity data from individual radars. The data span the period from May 5 to May 7 and cover the middle U.S. (Figure 2.1). There was a transitional period between May and August 2008 in which the NEXRAD network was upgraded for higher-resolution volume scans. During this period some data have an azimuth spacing of 0.5° and a slant range of 0.25 km, while other data have an azimuth spacing of 1° and a slant range of 1 km. We follow the method outlined in *Homeyer* (2014) to combine the individual volume scans into 3-D gridded radar reflectivity composites. The processed composites have a horizontal grid spacing of 0.02°, a vertical grid spacing of 1 km, and a time spacing of 5 minutes.

2.3 Lightning Data

Lightning data are provided by the ground-based U.S. National Lightning Detection Network (NLDN) which tracks lightning activities across the continental U.S.

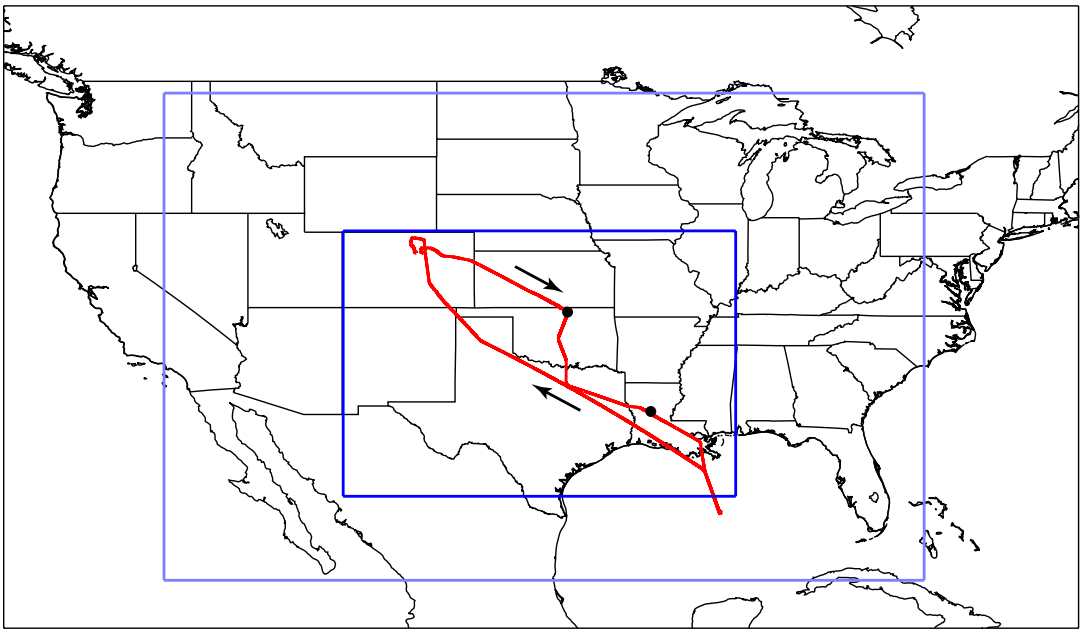

Figure 2.1: Map of the study area. The red curve is the aircraft flight path for Research Flight 8. Light and dark blue boxes indicate the outer and inner domains of the WRF model, respectively. The flight direction, and the locations of the two missed approaches are indicated by arrows and black dots respectively.

(CONUS) (*Orville*, 2008). The network consists of more than 114 lightning sensors. We use data that are reprocessed and archived for non-real-time users. The data contain date and time, location (in latitude and longitude), peak current (in kA), and strokes per flash (multiplicity) of each lightning event during the field campaign. Thunderstorm and flash detection efficiencies of the network are more than 99% and 95%, respectively.

2.4 Satellite Data

Water vapor, infrared and visible images are provided by the NOAA Geostationary Operational Environmental Satellite (GOES) system. The GOES images are used along with the radar to follow the evolution of the squall line system and convective outflow.

3. MODELS

We use the NCAR Weather Research and Forecasting (WRF) model with the Advanced Research WRF (ARW, version 3.2.1) dynamical solver to simulate the squall line observed during RF08. The model is configured with two domains (Figure 2.1) with two-way interaction between the domains. The horizontal grid spacing of the inner domain and outer domain are ∼3.0 km × ∼3.7 km and ∼9.1 km × ∼11.0 km respectively. The model has 45 vertical layers at full (mass) levels in η-coordinates from the ground to 50 hPa. The vertical spacing increases with altitude, ranging from 200 m in LT to 510 m in UT. Output is interpolated into other vertical coordinates when necessary. The model time step is 270 seconds (4.5 minutes).

The simulation is initialized with the National Centers for Environmental Prediction (NCEP) Eta/NAM 212 grid (40 km) 3-hour model analysis and run for a period of 42 hours from 12:00 UTC May 5, 2008 to 06:00 UTC May 7, 2008. The primary period of interest for this study is 00:00 UTC to 18:00 UTC May 6, which occurs 12 to 30 hours after the beginning of the simulation. To minimize time sampling errors in the trajectory calculations, model variables are archived at every time step (*Bowman et al.*, 2013).

Boundary conditions for the model outer domain come from the NCEP Eta/NAM 212 analysis and NOAA real time global (RTG) sea surface temperature data. Model variables in the outer domain are nudged to the Eta/NAM analysis throughout the simulation, while variables in the inner domain are only nudged for the first 6 hours. There is no nudging of temperature and moisture in the BL. Vertical velocity damping is applied to the uppermost 6 km in both domains for robustness. This damping reduces the reflection of gravity waves from the upper boundary. A set of physical

parameterization schemes is used to represent the sub-grid-scale processes in the model (Table 3.1). We use NCAR Command Language (NCL) utilities to compute the simulated radar reflectivity of the model for comparison with observations.

Because this study is concerned with convective transport, we trace transport pathways for selected air parcels using the TRAJ3D trajectory model (*Bowman*, 1993; *Bowman and Carrie*, 2002). Backward trajectories are computed offline using the simulated WRF wind fields saved at every time step. Given the source regions of the parcels from the back trajectories and the concentrations of trace gases from a profile measured by the GV as it descended from the lower stratosphere to the BL ahead of the squall line, we estimate the concentration of CO and NO_y in the outflow layers according to

$$C = f_{LS} \cdot C_{LS} + f_{UT} \cdot C_{UT} + f_{MT} \cdot C_{MT} + f_{LT} \cdot C_{LT} + f_{BL} \cdot C_{BL}. \qquad (3.1)$$

where f is fraction of parcels from each source region and C is concentration of a given species within those source regions. Source regions are designated as lower stratosphere (LS), upper troposphere (UT), middle troposphere (MT), lower troposphere (LT), and boundary layer (BL).

The NCEP Global Forecast System (GFS) model analysis is used to calculate the tropopause height. The model has 47 vertical layers in hybrid σ-pressure coordinate. The vertical grid spacing of the model output is 25 hPa between 100 and 1000 hPa, and gets smaller above 100 hPa. The horizontal grid spacing is $0.3125^\circ \times 0.3125^\circ$ ($\sim$35 km). The GFS analyses are available four times daily (0000, 0600, 1200, and 1800 UTC) (*Homeyer et al.*, 2010). The GFS tropopause is calculated by using the World Meteorological Organization (WMO) algorithm, which defines the tropopause to be the lowest altitude at which the average lapse rate decreases to 2°C km^{-1} on

Table 3.1: Physical parameterizations of the WRF model runs. The cumulus parameterization is only applied to the outer domain.

Type of parameterization	Schemes
Microphysics	Goddard six-species, single moment microphysics scheme (*Tao et al.*, 1989)
Cumulus	Betts-Miller-Janjic (BMJ) scheme (*Janjić*, 1994)
Planetary boundary layer	Yonsei University (YSU) scheme (*Hong et al.*, 2006)
Land surface	Noah land-surface model (*Ek et al.*, 2003)
Surface layer	Eta surface layer scheme (*Janjić*, 1996)
Longwave radiation	Rapid Radiative Transfer Model (RRTM) (*Mlawer et al.*, 1997)
Shortwave radiation	Goddard shortwave scheme (*Chou and Suarez*, 1994)

the condition that the average lapse rate from this height to any level within the next higher 2 km does not exceed 2°C km^{-1} (*World Meteorological Organization*, 1957).

4. RESULTS

4.1 START08 Research Flight 8

Research Flight 8 (RF08) took place on May 6, 2008 from 14:55 UTC until 21:32 UTC (Figure 2.1). The aircraft took off from Colorado and flew out over the Gulf of Mexico before returning to Colorado. The aircraft descended from the LS and executed a missed approach at Ponca City, OK. It then ascended once more into the LS, flew above a weakening squall line located in north Texas and Oklahoma, and then descended to execute a second missed approach at Alexandria, LA. The two missed approaches are indicated by black dots (Figure 2.1). The descent to the second missed approach provided a profile of the outflow from the squall line and the environment into which the squall line was propagating.

Several quantities observed by the aircraft during the squall line overflight and descent are plotted as a function of time (Figure 4.1). Figure 4.1a shows the tropopause height at the aircraft location from the GFS analysis (gray + colors) and the aircraft altitude (black + colors). The colors indicate possible layers identified subjectively based on the trace species shown in Figures 4.1b and c. Two potential convective outflow layers just below the tropopause are colored red and green, respectively. The remaining colors indicate the upper troposphere (UT, yellow), middle troposphere (MT, purple), lower troposphere (LT, orange), and boundary layer (BL, blue). Note that the yellow layer represents the unperturbed and background upper troposphere air compared to the red and green layers.

The O_3 (black + colors) and CO (gray + colors) data show the descent from just above the tropopause into the troposphere near 16:59 UTC (Figure 4.1b). There is a transitional mixing region approximately 150 m thick between the stratosphere and

troposphere (12.786 to 12.632 km altitude or 181.1 to 188.9 hPa) within which O_3 and CO rapidly change from stratospheric to tropospheric values. The relationship between O_3 and CO is quite linear within the mixing layer.

The NO and NO_y data in particular suggest the presence of two distinct outflow layers in the UT. These are colored red and green (Figure 4.1c). The concentrations in these two layers are very different from the observations in the MT and LT, but are of the same order as in the BL, which is sampled near 17:20 UTC. The upper layer includes the shallow stratosphere-troposphere transition layer and extends from 12.786 km to 11.739 km ($\sim$1.0 km from 184 to 218 hPa); the lower layer is deeper and extends from 11.739 to 7.542 km ($\sim$4.2 km from 218 to 400 hPa). For simplicity, in what follows we refer to these as the red and green layers, respectively.

4.2 Evolution of the Squall Line

The evolution of the squall line system observed during RF08 can be seen in NEXRAD data (left) and the WRF simulation (right) (Figure 4.2). The convective system of interest is identified by arrows in each panel. The squall line starts as isolated convective cells on May 5 (Figure 4.2a). WRF produces similar isolated convection through the evening (Figure 4.2b). The isolated storm cells move eastward and begin to merge around 23:00 UTC. An organized squall line forms by 08:00 UTC May 6, 2008.

A leading-convective/trailing-stratiform squall line can be recognized with a north-east–southwest orientation and column-maximum radar reflectivity at the leading edge exceeding 50 dBZ at 10:20 UTC May 6, 2008 (Figure 4.2c). The simulated squall line has a similar intensity and orientation but propagates slightly faster than its observed counterpart (Figure 4.2d). To improve the match between observations and simulation, the simulation is shifted 7 time steps (31.5 minutes) backward rel-

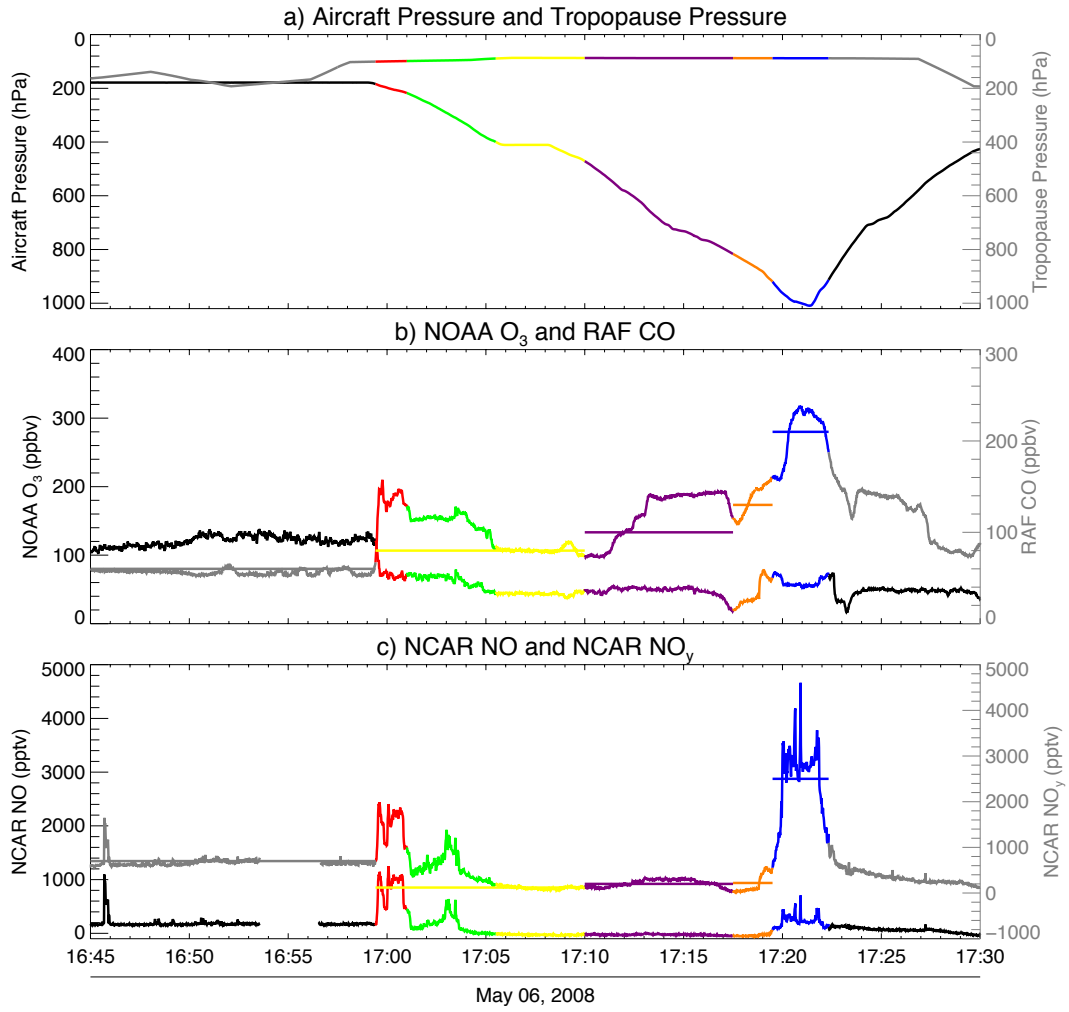

Figure 4.1: a) Tropopause height (gray + colors) and aircraft altitude (black + colors); b) ozone (black + colors) and carbon monoxide (gray + colors); c) NO (black + colors) and NO_y (gray + colors). Various subjectively identified layers are color-coded in all three panels: upper outflow layer (red), lower outflow layer (green), upper troposphere (yellow), middle troposphere (purple), lower troposphere (orange), and boundary layer (blue). The horizontal lines in panels b and c are the representative values for each layer used to predict values in the red and green layers in combination with the back trajectories. The values are tabulated in Table 4.1.

ative to the observations. That is, we compare observations for a given time with the simulation from 31.5 minutes earlier. There is an irregular mesoscale convective system moving eastward from north Mexico to south Texas.

At 14:35 UTC, the simulated squall line is somewhat stronger than the observations (Figures 4.2e and f). The aircraft flew just above the top of the outflow cirrus near 17:00 UTC on May 6 and then descended to make a missed approach in Louisiana near 17:21 UTC (Figure 4.2g). At the time of the overflight and descent, the simulated squall line is still somewhat stronger than the observations, but the structure is similar (Figure 4.2h). After adjusting for the slightly faster propagation speed of the squall line in the simulation, we find the horizontal structure and location of the squall line in the WRF simulation to be consistent with the NEXRAD data.

Figure 4.3 shows vertical sections of the simulated and observed radar reflectivity several hours before and at the time of the aircraft overflight along the lines labeled A–B in Figures 4.2e and f. In Figures 4.3c and d, the location of the aircraft at the respective time is indicated by a plus sign. At the earlier times (Figures 4.3a and b), the detectable echo tops reach near 11 km attitude, which is the boundary between the green and red layers. As the storm weakens the depth of the convection decreases, but the simulated storm weakens more slowly and remains somewhat deeper and broader than the observations. Although the aircraft overflew the southern end of the squall line only, the simulated storm is stronger than the observations in other parts of squall line as well by translating the line A–B northward (not shown). The vertical sections suggest that the air in the green and red layers was transported to the upper troposphere several hours before it was observed by the aircraft. This is confirmed by the trajectory studies in the next section.

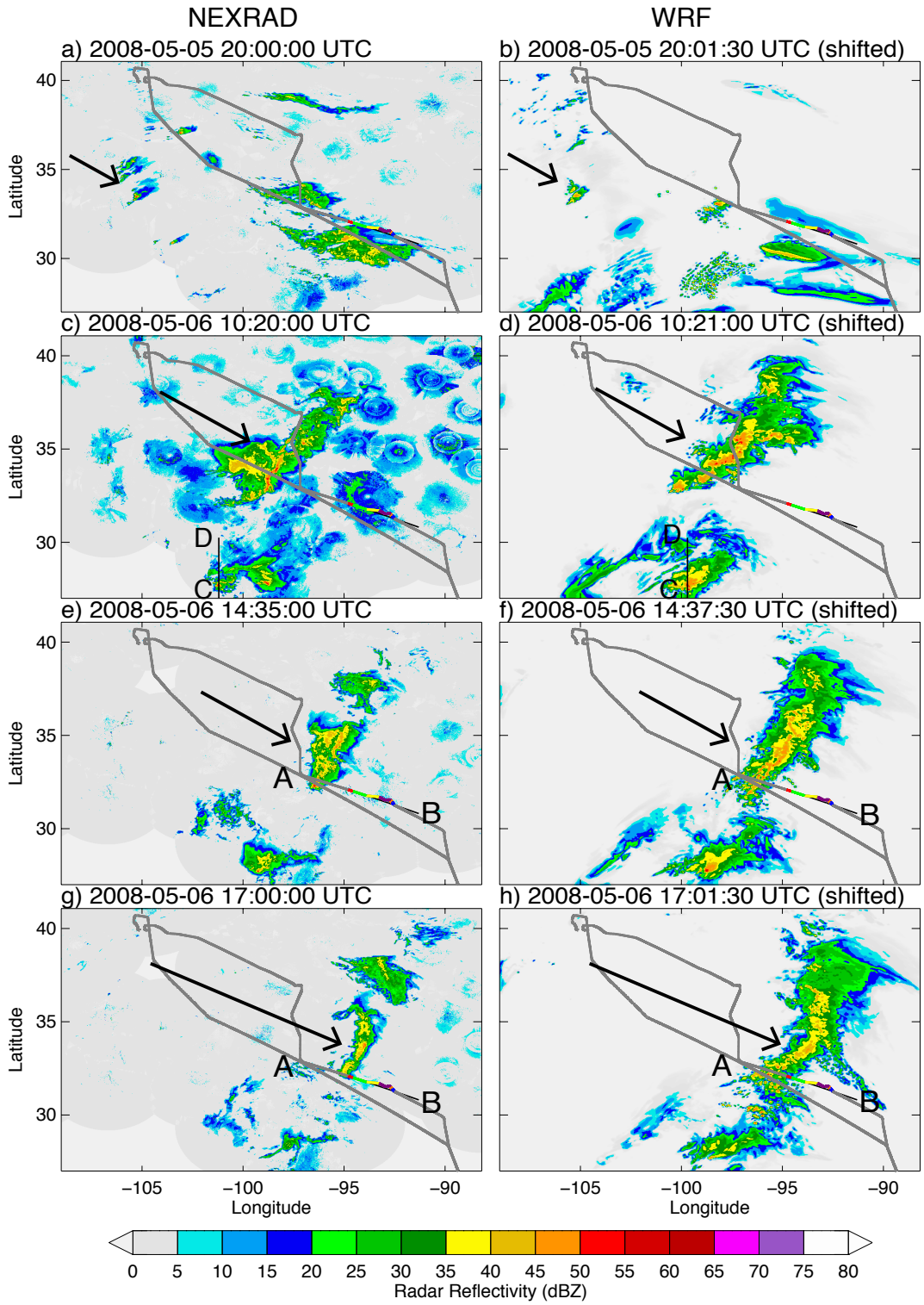

Figure 4.2: Maps showing the evolution of the squall line in NEXRAD and WRF (arrows). The time in the WRF simulation is shifted back by seven time steps (31.5 minutes).

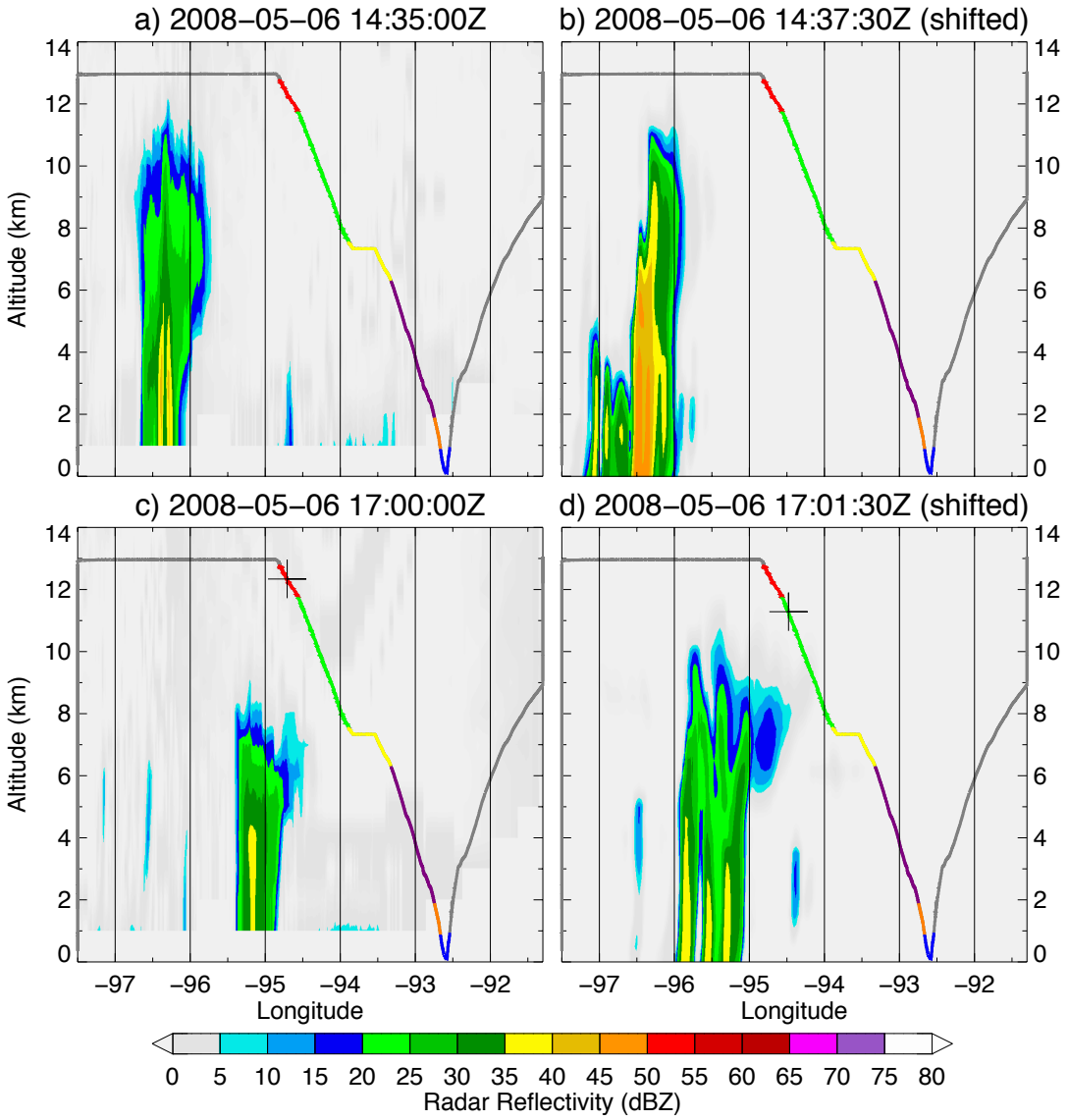

Figure 4.3: Vertical structure of the observed (a and c) and simulated (b and d) radar reflectivity along lines labeled A–B in Figures 4.2 e–h respectively. The plus sign indicates the location of the aircraft. Colors along the flight track indicate the layers as shown in Figure 4.1. The time in WRF simulation is shifted back by seven time steps (31.5 minutes).

4.3 Trajectory Analysis

In order to determine the sources of air in the green and red outflow layers, back trajectories are computed for a grid of particles initialized in the volume surrounding the three-dimensional aircraft flight path.

4.3.1 Lower Outflow Layer

For the green layer the initial volume of particles lies between 93.9° and 94.5°W, 31.7° and 32.0°N, and $\eta = 0.3650$ and 0.18. With a grid spacing of 0.1° × 0.1° × 0.0025 η (approximately 9.5 km × 11 km × 64 m in this part of UT), the volume for the green layer includes $7 \times 4 \times 75 = 2100$ particles.

Analysis of the back trajectories of the air in the green layer reveals that parcels arrive through three different pathways: 40% is convected to the UT by the squall line that the aircraft overflew immediately before descending through the outflow layer; 8% is convected by a separate MCS located in north Mexico; and 52% is environmental air from the UT and MT.

Figure 4.4 shows a representative trajectory for a parcel convected by the squall line. For clarity, only a single trajectory is plotted. Other trajectories in this group are tightly bunched around this trajectory. Note that while the plotted trajectory shows many hours of motion by the parcel, the simulated radar map is for a single time, in this case for 14:15 UTC May 6, which is during the interval when the parcels ascend rapidly in the updraft. The portion of the trajectory within ±45 minutes of the radar time is indicated by black dots plotted along the trajectory. The parcels in this group come from the LT and MT in south Texas and from the BL and LT in north Mexico. After moving generally northward at low levels and northeastward at middle level, they ascend to the UT in the updrafts near the southwestern end of the squall line. This occurs approximately 2.75 hours before they reach the volume

sampled by the aircraft near 17:00 UTC.

The second convective system responsible for transporting air to the green layer (8%) is an irregular MCS in north Mexico. This system is seen in Figure 4.2 in both the NEXRAD data and the WRF simulation. This MCS moves from north Mexico to south Texas and dies out around 18 UTC May 6. Figure 4.5 shows a representative example from those trajectories. In this case the radar map is for 00:00 UTC May 6, which is during the interval when the parcels ascended rapidly in the updraft. The parcels in this group come from north Mexico and are initially located at levels from the BL to the MT. After ascending to the UT in the updrafts of the southern MCS, they move generally northeastward. This occurs approximately 17 hours before the volume is sampled by the aircraft, which is 14 hours before the convective transport by the squall line. There is no indication of lightning occurring in this MCS at this time.

The distributions of sources and transport pathways for parcels in the green layer are given in Figure 4.6 as a function of altitude. Parcels that are transported from the squall line (SQ, magenta), southern MCS (MCS, cyan) and other (light gray) show that the two MCSs account for convecting more than 50% of parcels above $\eta = 0.29$ (Figure 4.6a). The parcels can also be classified by their source regions. In Figure 4.6b, parcels that come from the UT, MT, LT, and BL are colored in yellow, purple, orange, and blue respectively. At all levels the sources are dominated by air from the middle and lower troposphere.

Using Equation (3.1) and the parcel source region fractions from Figure 4.6b, we estimate the concentrations of CO and NO_y as a function of altitude assuming that both CO and NO_y are conserved. The assumed values for the initial concentrations in the source regions are plotted as horizontal lines on the aircraft time series in Figures 4.1b and c and are given in Table 4.1. The predicted values for each of the

Table 4.1: Layer averaged concentrations of CO and NO_y in the source regions used with the trajectories to predict the measured values.

Source region	CO (ppbv)	NO_y (pptv)
Lower stratosphere (LS)	60	700
Upper troposphere (UT)	80	120
Middle troposphere (MT)	100	200
Lower troposphere (LT)	140	220
Boundary layer (BL)	210	2500

5 layers in Figure 4.6b are plotted with crosses and dashed lines in Figure 4.6c.

The estimated and observed CO concentrations generally agree quite well and are nearly constant in the vertical. The estimated NO_y concentration agrees well at upper and lower levels, but fails to reproduce the broad peak in NO_y in the middle of the green layer around $\eta = 0.255$. This sub-layer also shows up distinctly in a scatterplot of NO_y and CO values measured between 16:45 and 17:30 UTC May 6 (Figure 4.7). It is unlikely that the peak in NO_y is due to transport from the boundary layer, because CO remains constant in this layer. If the air came from the BL, then CO should increase along with NO_y. We note instead that at the time the parcels ascend in the updrafts, lightning occurs in the squall line, indicated by gray crosses in Figure 4.4. An expanded map of the region (Figure 4.8) near the updrafts in Figure 4.4 shows all of the trajectories between $\eta = 0.23$ and 0.28 along with observed lightning occurring while the parcels are in the updrafts (13:30 UTC to 15:00 UTC). There is no lightning activity associated with the convection in the southern MCS case.

4.3.2 Upper Outflow Layer

For the red layer the initial volume of particles lies between 94.6° and 94.9°W, 31.9° and 32.2°N, and $\eta = 0.1775$ and 0.14. With a grid spacing of 0.1° × 0.1° ×

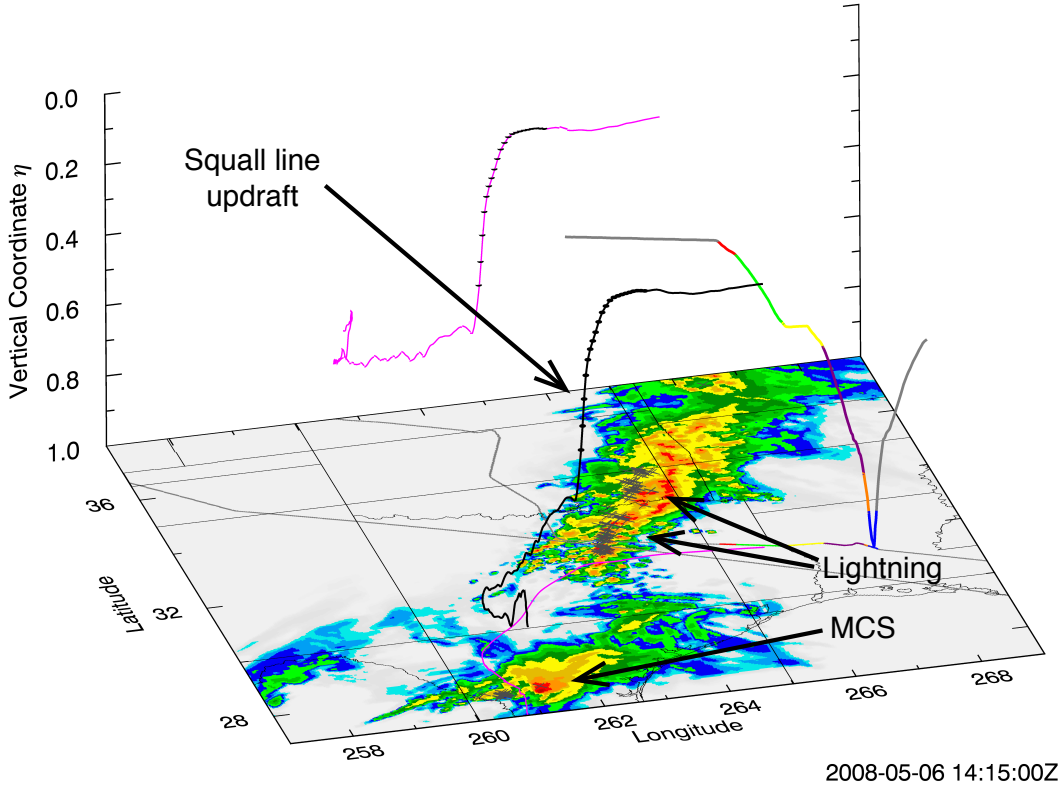

Figure 4.4: A typical 24-hour back trajectory for air parcels convected by the squall line. The 3-D trajectory is shown in black; longitude-latitude and longitude-altitude projections of the trajectory are plotted in magenta. Near the time of the simulated radar map (14:15 UTC May 6, 2008) the parcels ascend rapidly in updrafts within the squall line. This interval is indicated by black dots plotted on the trajectories. Observed lightning flashes occurring near this time are indicated by gray crosses superimposed on the radar map. The position of the MCS at this time is also indicated.

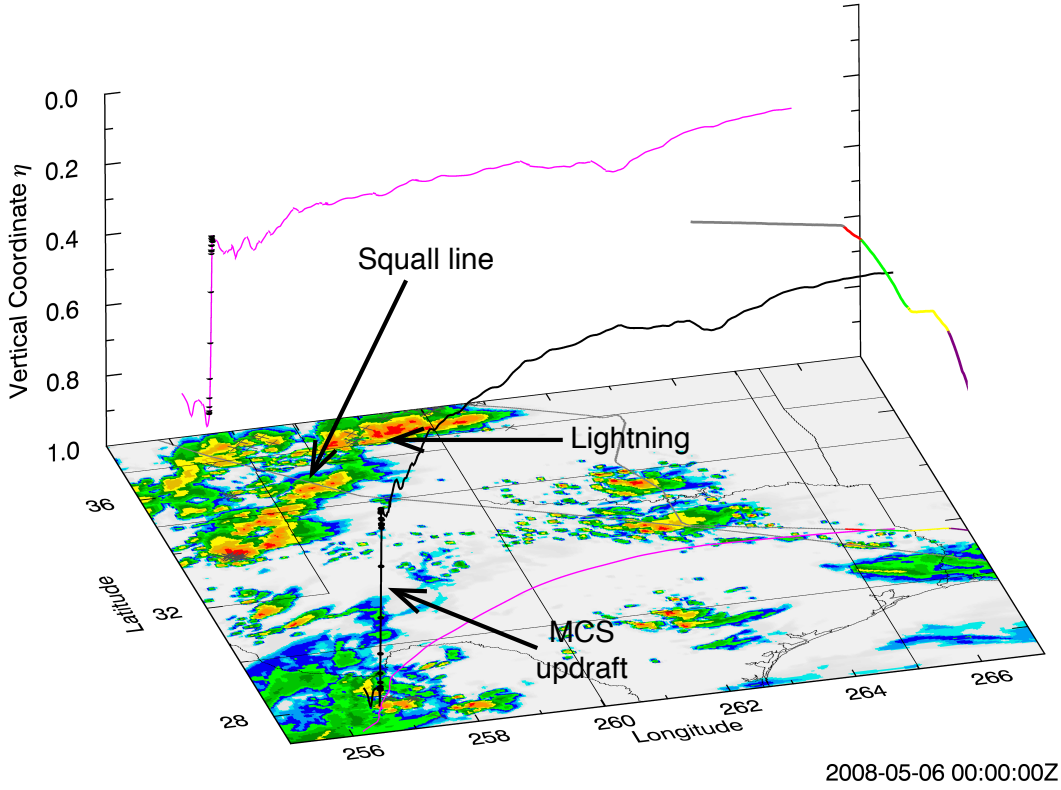

Figure 4.5: A typical 24-hour back trajectory for air parcels convected by the southern MCS. The 3-D trajectory is shown in black; longitude-latitude and longitude-altitude projections of the trajectory are plotted in magenta. Near the time of the simulated radar map (00:00 UTC May 6, 2008) the parcels ascend rapidly in updrafts within the MCS. This interval is indicated by black dots plotted on the trajectories. Observed lightning flashes occurring near this time are indicated by gray crosses superimposed on the radar map. The position of the squall line at this time is also indicated.

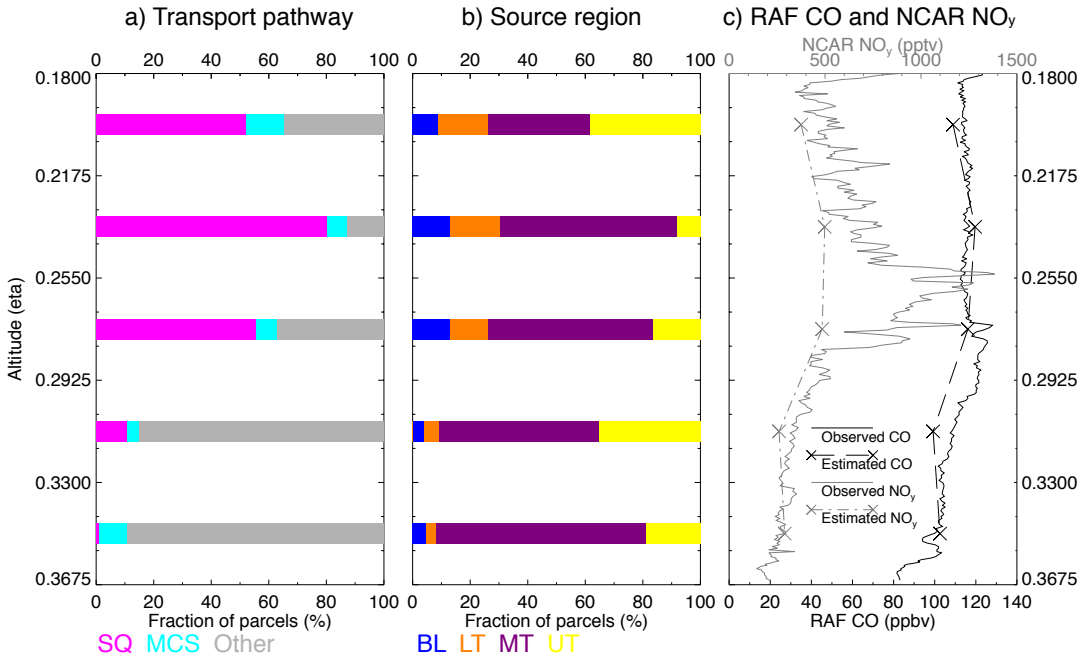

Figure 4.6: Lower (green) outflow layer as a function of altitude. a) Fraction of parcels by transport pathway: squall line (magenta), southern MCS (cyan), and other (light gray). b) Fraction of parcels by source region: upper troposphere (yellow), middle troposphere (purple), lower troposphere (orange), and boundary layer (blue). c) Concentration of CO and NO_y: observed (black) and estimated (black crosses and dashed line) CO, and observed (gray) and estimated (gray crosses and dashed line) NO_y.

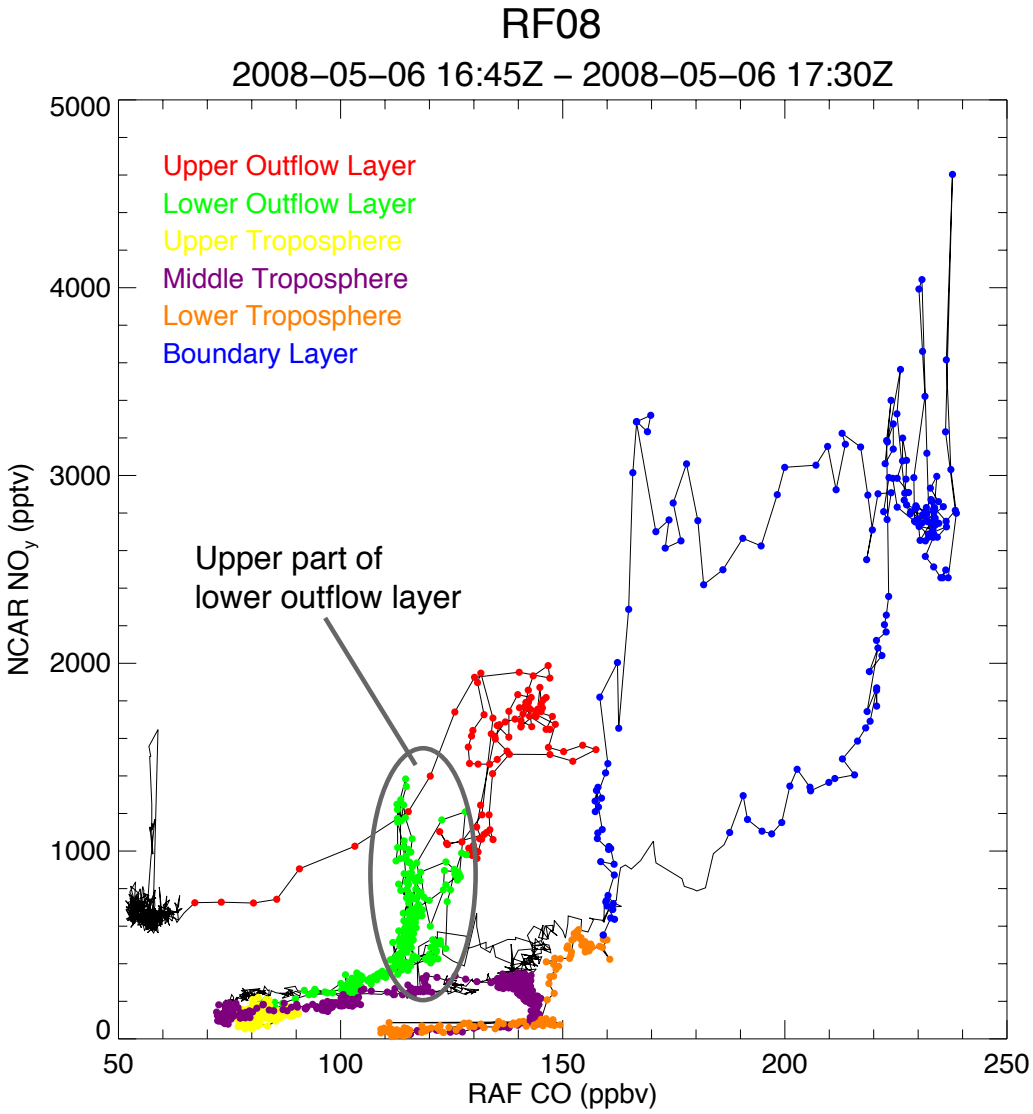

Figure 4.7: Tracer-tracer plot for NO_y against CO between 16:45 UTC and 17:30 UTC May 6: upper outflow layer (red), lower outflow layer (green), upper troposphere (yellow), middle troposphere (purple), lower troposphere (orange), and boundary layer (blue).

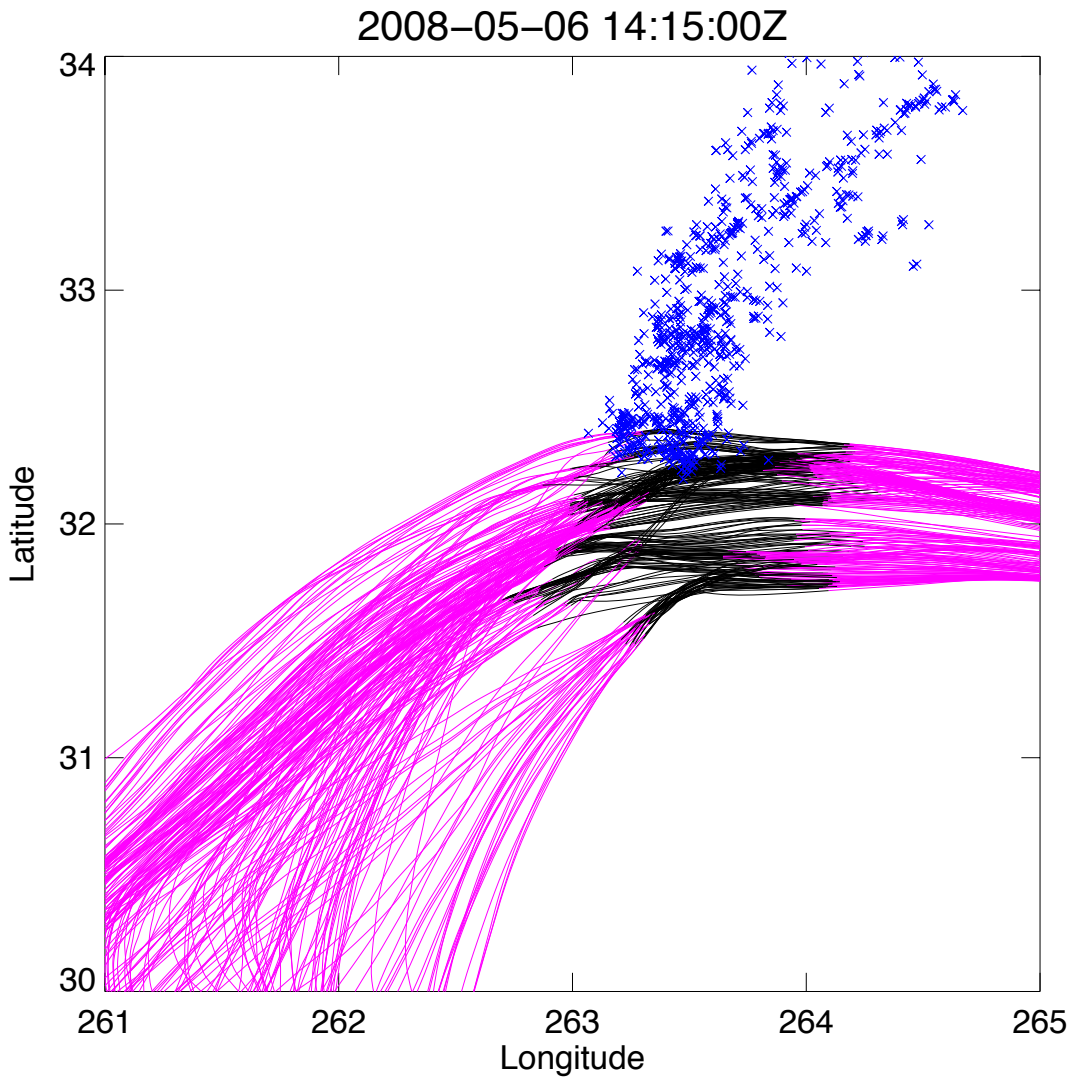

Figure 4.8: Expanded map of parcel trajectories that are convected by the squall line in the lower outflow layer. The trajectories are selected with those end up reaching between $\eta = 0.23$ and 0.27 in the lower outflow layer. The black segments of the parcel tracks indicate the convective updrafts. The blue crosses are the locations of lightning flashes occurring at this time (13:30 UTC to 15:00 UTC).

0.0025 η (approximately 9.5 km $\times$ 11 km $\times$ 72 m in this part of UT), the volume for the red layer includes $4 \times 4 \times 16 = 256$ particles.

Analysis of the back trajectories of the air in the red layer reveals that parcels arrive through two different pathways: 23% is convected to the UT by the MCS located in south Texas that also contributed to the green layer, and 77% is environmental air from the LS and UT. Figure 4.9 shows a representative trajectory for a parcel convected by the MCS. The simulated radar map is for 10:21 UTC May 6. The portion of the trajectory within $\pm$45 minutes of the radar time is indicated by black dots plotted along the trajectory. The parcels in this group come from south Texas and are initially located at levels from the BL to the MT. After ascending to the UT in the updrafts of the MCS, they move generally northeastward. This occurs approximately 6.5 hours before the volume is sampled by the aircraft. Although the MCS responsible for this air is the same as that in Figure 6, the elapsed time between the ascent in convection and the measurement by the aircraft is shorter due to vertical shear in the background flow.

The distributions of sources and transport pathways for parcels in the red layer are given in Figure 4.10 as a function of altitude. Parcels transported by the MCS (cyan) account more than 50% of the parcels between $\eta = 0.16$ and 0.17 (Figure 4.10a). In Figure 4.10b, parcels that come from the UT, MT, LT, and BL are colored using the same color scheme as in Figure 4.6 while those come from the lower stratosphere (LS) are colored in dark gray. Except at the very top of the profile, where most of the parcels are from the lower stratosphere, most parcels come from the UT or the MCS. Predicted concentrations of CO and NO_y as a function of altitude in the red layer are plotted in Figure 4.10c along with the observations. The predicted CO concentrations are somewhat low throughout the layer, particularly between $\eta = 0.145$ and 0.155. Predicted NO_y values are much lower than observations throughout the layer and do

not capture the minimum in NO_y near $\eta = 0.155$.

The parcel trajectories indicate that air in the upper part of the red layer is entirely from the lower stratosphere and upper troposphere, but CO is near 140 ppbv and NO_y is over 1500 pptv in the observations. At lower levels, where a substantial fraction of the air parcels come from the MT, LT, and BL, CO is low by 15 to 30%, but NO_y is low by a factor of 6. Figure 4.11 shows vertical sections of the simulated and observed radar reflectivity of the MCS at the time of the convective transport (Figure 4.9) along the lines labeled C–D in Figures 4.2 c and d. Although the simulated MCS appears somewhat larger and more intense in the Figures 4.2 c and d, the observed echo tops reach 15 km whereas those in model reach only to 12 km, which is the boundary between the red and green layers. These results together suggest that the convective transport to the red layer as a whole is underestimated by the model, and that model convection does not extend quite high enough (up to $\eta = 0.155$ in Figure 4.10b), leading to the greater under-prediction of CO and NO_y in the upper part of the layer. This is different from the green layer, where the observed and simulated storms have similar intensities and echo top heights and the concentrations are well predicted by the trajectories and simple mixing model. It might also be the case that we underestimate the CO concentrations in the middle and lower tropospheric source regions. The large NO_y discrepancy, however, seems to be due to other sources, such as lightning. Lightning is observed to occur during the time period these parcels ascend in the updrafts of the southern MCS. An expanded map of the region (Figure 4.12) near the updrafts in Figure 4.9. The combination of the lack of a lightning source and of insufficient convective transport to the top of the red layer explain the poor prediction of NO_y.

Thus, the echo top height might be one of the most important criteria for a successful storm and chemical transport simulation.

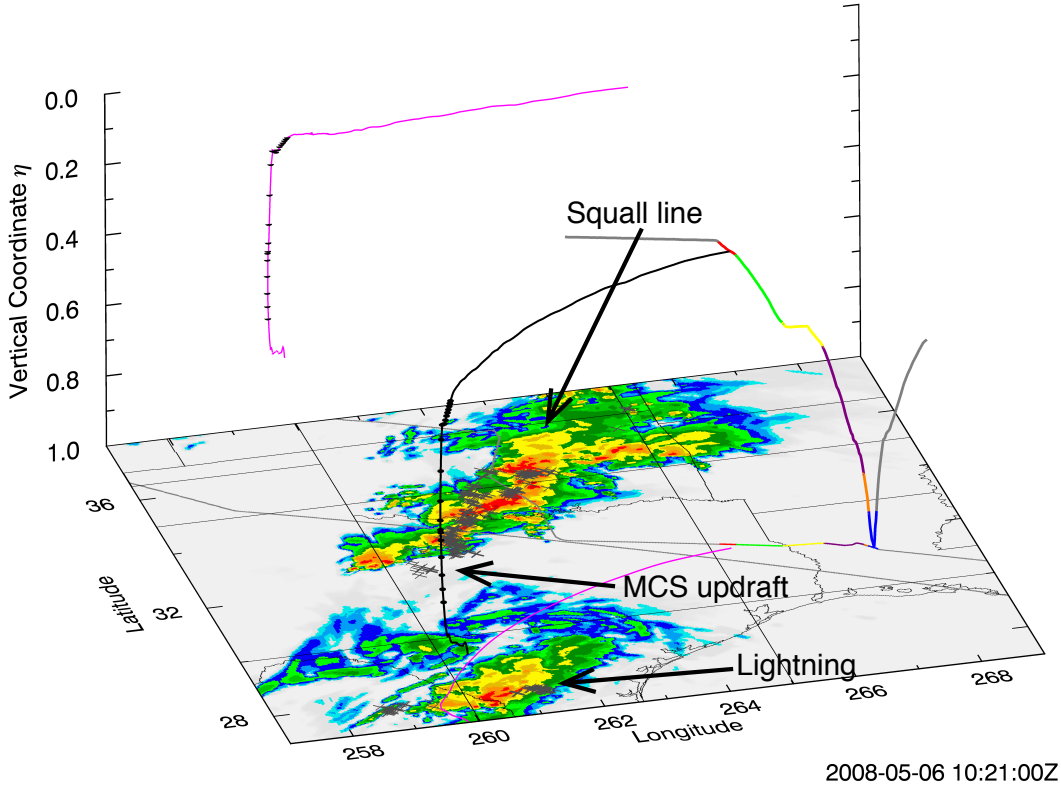

Figure 4.9: A typical 24-hour back trajectory for air parcels convected by the southern MCS. The 3-D trajectory is shown in black; longitude-latitude and longitude-altitude projections of the trajectory are plotted in magenta. Near the time of the simulated radar map (10:21 UTC May 6, 2008) the parcels ascend rapidly in updrafts within the MCS. This interval is indicated by black dots plotted on the trajectories. Observed lightning flashes occurring near this time are indicated by gray crosses superimposed on the radar map. The position of the squall line at this time is also indicated.

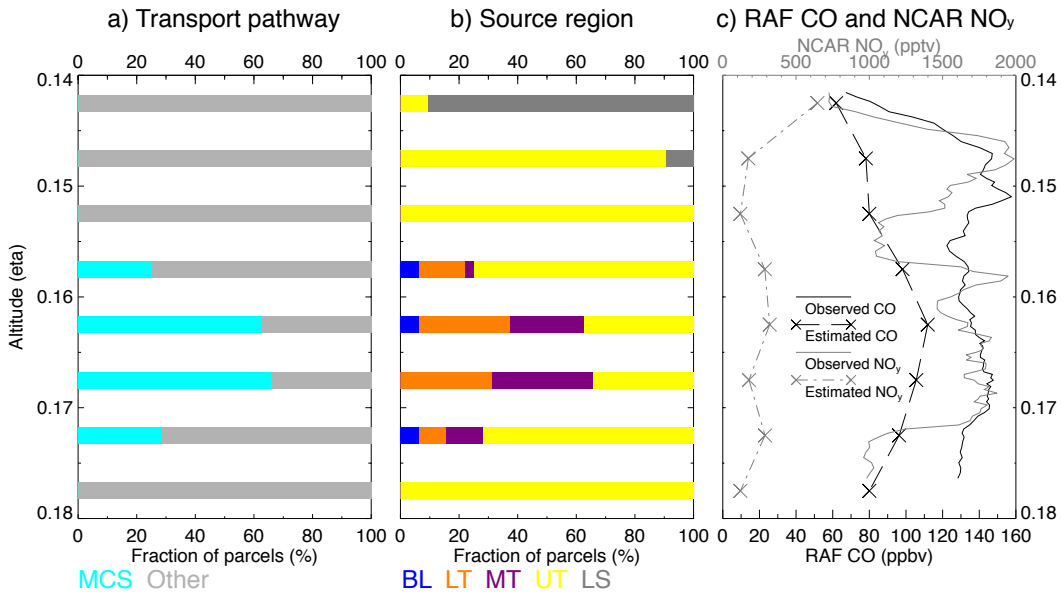

Figure 4.10: Upper (red) outflow layer as a function of altitude. a) Fraction of parcels by transport pathway: southern MCS (cyan), and other (light gray). b) Fraction of parcels by source region: lower stratosphere (dark gray), upper troposphere (yellow), middle troposphere (purple), lower troposphere (orange), and boundary layer (blue). c) Concentration of CO and NO_y: observed (black) and estimated (black crosses and dashed line) CO, and observed (gray) and estimated (gray crosses and dashed line) NO_y.

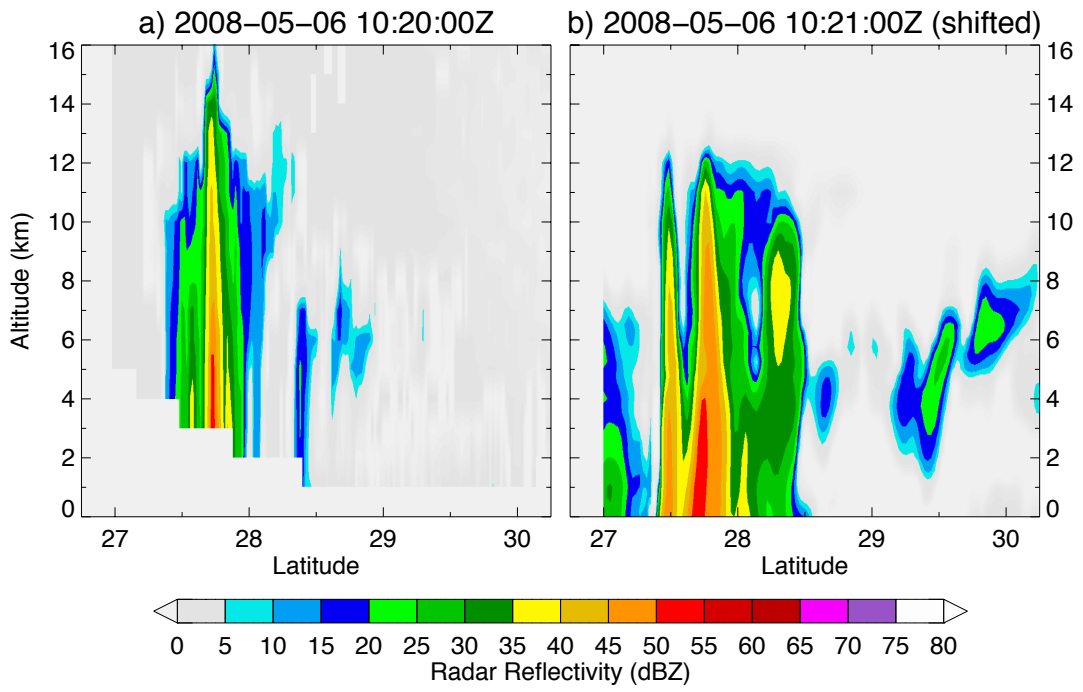

Figure 4.11: Vertical structure of the observed (a) and simulated (b) radar reflectivity along lines labeled C–D in Figures 4.2 c and d respectively. The time in WRF simulation is shifted back by seven time steps (31.5 minutes).

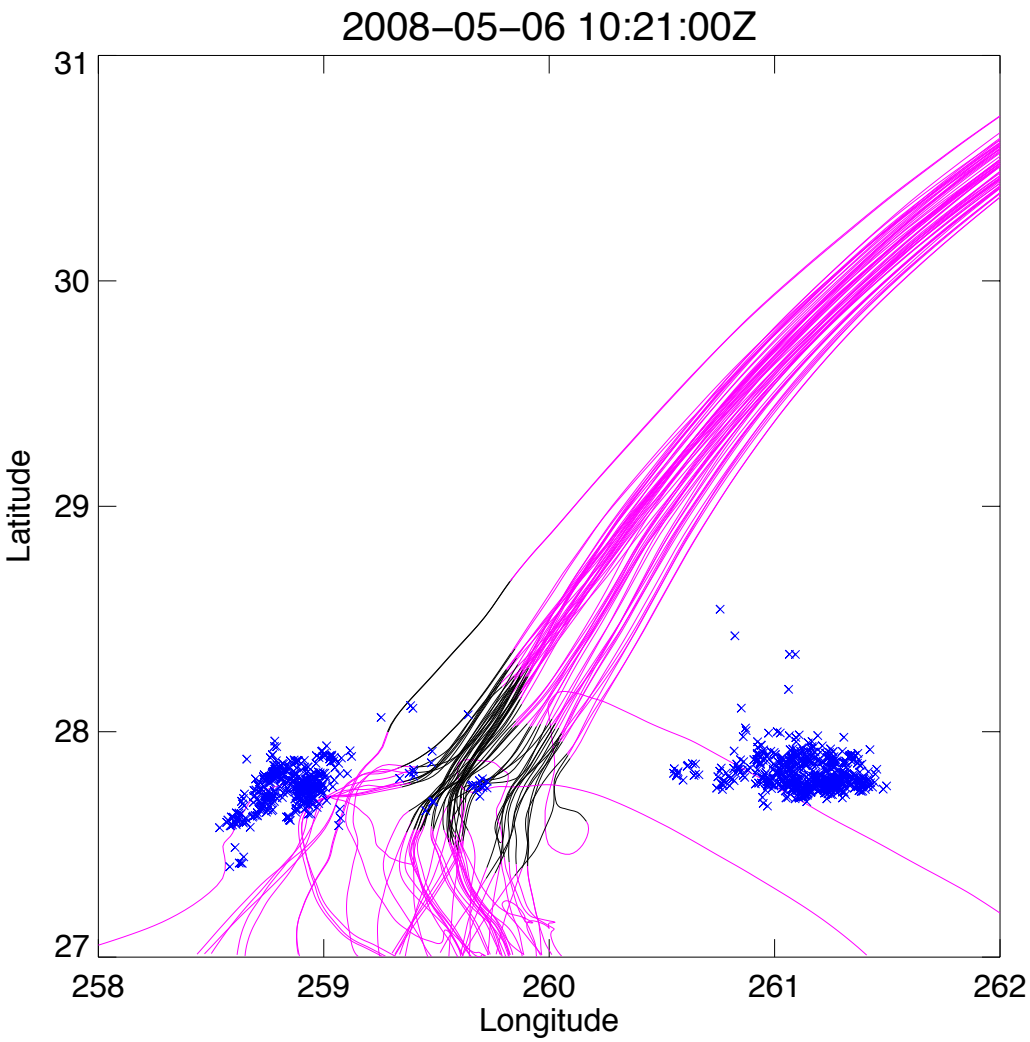

Figure 4.12: Expanded map of parcel trajectories that are convected by the southern MCS in the upper outflow layer. The trajectories are selected with those end up reaching between $\eta = 0.155$ and 0.175 in the upper outflow layer. The black segments of the parcel tracks indicate the convective updrafts. The blue crosses are the locations of lightning flashes occurring at this time (09:36 UTC to 11:06 UTC).

5. CONCLUSIONS

This study attempts to determine the origin and transport pathways of air in the upper-tropospheric outflow from a squall line observed in north Texas during the START08 field program. The outflow air, which is located immediately below the tropopause, is characterized by two distinct layers with high values of CO and NO/NO_y. Air parcel trajectories for the observed outflow layers are computed using three-dimensional wind fields from a high-resolution simulation with the Weather Research and Forecasting (WRF) model. The model is initialized more than a day prior to the time the aircraft observations were made and integrated forward using initial and boundary conditions taken from operational analyses. The model reproduces the initiation, growth, and decay phases of the observed convective systems with good fidelity. The primary differences between the model and observations are that the simulated squall line propagates eastward slightly faster and weakens more slowly during the later stages than is observed.

Back trajectories computed with the WRF wind fields show that the air in the outflow layers is a mixture of air parcels with sources ranging from the boundary layer to the upper troposphere. The trajectories also show that significant contributions to the outflow air did not come from the nearby squall line, but instead were transported a substantial distance northward and eastward from the outflow of a mesoscale convective system located in north Mexico and south Texas. In the lower (green) outflow layer 52% of the air parcels are environmental air from the middle and upper troposphere, while 40% and 8% of the parcels respectively are transported vertically by convection within the squall line and MCS. The observed concentrations of CO and NO_y in the lower outflow layer are predicted as a function

of altitude using a simple model based on the observed aircraft profiles of CO and NO_y and the contributions from different source altitudes estimated from the back trajectories. The model, which assumes that CO and NO_y are conserved during transport, captures the vertical profile of CO throughout the lower outflow layer and of NO_y at the bottom and top of the layer, but it fails to reproduce a localized layer of enhanced NO_y. Data from the NLDN show that lightning was occurring at the time air parcels were transported vertically within the squall line to the lower outflow layer. Based on this we conclude that roughly half of the NO_y in the lower outflow layer was transported from the boundary layer and lower troposphere, while the other half was produced by lightning with the convective updrafts that fed the outflow.

In the upper outflow layer, 23% of the particles are transported by the MCS and the remaining 77% are environmental air from the LS and UT. Although the upper outflow layer is immediately downwind of the squall line system, the convective transport to the this layer did not occur within the squall line, but instead happened in the updrafts of an MCS in south Texas. This air was then transported northward to the upper outflow layer by the environmental flow. In the upper outflow layer the model underestimates CO by about 15 to 30% and NO_y by as much as a factor of 6. The discrepancies in the upper outflow layer appear to be largely due to an underestimate of the vertical transport to the very top of the troposphere by the MCS and to the lack of a lightning source for NO_y.

These results demonstrate that accurate, high-resolution, three-dimensional simulations of complex convective events are possible; and that given an accurate simulation of the meteorological environment, it is possible to interpret high-resolution observations of important trace gases in terms of transport pathways and sources, such as lightning. While the meteorological simulation in this case is generally quite

good, the simulated MCS in south Texas fails to produce sufficient convective transport to the very top of the troposphere, leading to an underestimate of CO and NO_y in the upper outflow layer.

REFERENCES

Barth, M. C., S.-W. Kim, C. Wang, K. E. Pickering, L. E. Ott, G. Stenchikov, M. Leriche, S. Cautenet, J.-P. Pinty, C. Barthe, C. Mari, J. H. Helsdon, R. D. Farley, A. M. Fridlind, A. S. Ackerman, V. Spiridonov, and B. Telenta (2007), Cloud-scale model intercomparison of chemical constituent transport in deep convection, *Atmos. Chem. Phys.*, *7*(18), 4709–4731, doi:10.5194/acp-7-4709-2007.

Bertram, T. H., A. E. Perring, P. J. Wooldridge, J. D. Crounse, A. J. Kwan, P. O. Wennberg, E. Scheuer, J. Dibb, M. Avery, G. Sachse, S. A. Vay, J. H. Crawford, C. S. McNaughton, A. Clarke, K. E. Pickering, H. Fuelberg, G. Huey, D. R. Blake, H. B. Singh, S. R. Hall, R. E. Shetter, A. Fried, B. G. Heikes, and R. C. Cohen (2007), Direct measurements of the convective recycling of the upper troposphere, *Science*, *315*(5813), 816–820, doi:10.1126/science.1134548.

Bowman, K. P. (1993), Large-scale isentropic mixing properties of the Antarctic polar vortex from analyzed winds, *J. Geophys. Res.*, *98*(D12), 23,013–23,027, doi:10.1029/93JD02599.

Bowman, K. P., and G. D. Carrie (2002), The mean-meridional transport circulation of the troposphere in an idealized GCM, *J. Atmos. Sci.*, *59*(9), 1502–1514, doi:10.1175/1520-0469(2002)059⟨1502:TMMTCO⟩2.0.CO;2.

Bowman, K. P., J. C. Lin, A. Stohl, R. Draxler, P. Konopka, A. Andrews, and D. Brunner (2013), Input data requirements for Lagrangian trajectory models, *Bull. Amer. Meteor. Soc.*, *94*(7), 1051–1058, doi:10.1175/BAMS-D-12-00076.1.

Bradshaw, J., D. Davis, G. Grodzinsky, S. Smyth, R. Newell, S. Sandholm, and S. Liu

(2000), Observed distributions of nitrogen oxides in the remote free troposphere from the NASA Global Tropospheric Experiment Programs, *Rev. Geophys.*, *38*(1), 61–116, doi:10.1029/1999RG900015.

Chou, M.-D., and M. J. Suarez (1994), An efficient thermal infrared radiation parameterization for use in general circulation models, *NASA Tech. Memo. 104606*, Goddard Space Flight Center.

Crum, T. D., R. L. Alberty, and D. W. Burgess (1993), Recording, archiving, and using WSR-88D data, *Bull. Amer. Meteor. Soc.*, *74*(4), 645–653, doi:10.1175/1520-0477(1993)074⟨0645:RAAUWD⟩2.0.CO;2.

Crutzen, P. J., and J. Lelieveld (2001), Human impacts on atmospheric chemistry, *Annu. Rev. Earth Planet. Sci.*, *29*(1), 17–45, doi:10.1146/annurev.earth.29.1.17.

DeCaria, A. J., K. E. Pickering, G. L. Stenchikov, J. R. Scala, J. L. Stith, J. E. Dye, B. A. Ridley, and P. Laroche (2000), A cloud-scale model study of lightning-generated NO_x in an individual thunderstorm during STERAO-A, *J. Geophys. Res.*, *105*(D9), 11,601–11,616, doi:10.1029/2000JD900033.

Dickerson, R. R., G. J. Huffman, W. T. Luke, L. J. Nunnermacker, K. E. Pickering, A. C. D. Leslie, C. G. Lindsey, W. G. N. Slinn, T. J. Kelly, P. H. Daum, A. C. Delany, J. P. Greenberg, P. R. Zimmerman, J. F. Boatman, J. D. Ray, and D. H. Stedman (1987), Thunderstorms: An important mechanism in the transport of air pollutants, *Science*, *235*(4787), 460–465, doi:10.1126/science.235.4787.460.

Dye, J. E., B. A. Ridley, W. Skamarock, M. Barth, M. Venticinque, E. Defer, P. Blanchet, C. Thery, P. Laroche, K. Baumann, G. Hubler, D. D. Parrish, T. Ryerson, M. Trainer, G. Frost, J. S. Holloway, T. Matejka, D. Bartels, F. C. Fehsenfeld, A. Tuck, S. A. Rutledge, T. Lang, J. Stith, and R. Zerr (2000), An overview

of the Stratospheric-Tropospheric Experiment: Radiation, Aerosols, and Ozone (STERAO)-deep convection experiment with results for the July 10, 1996 storm, *J. Geophys. Res.*, *105*(D8), 10,023–10,045, doi:10.1029/1999JD901116.

Ek, M. B., K. E. Mitchell, Y. Lin, E. Rogers, P. Grunmann, V. Koren, G. Gayno, and J. D. Tarpley (2003), Implementation of noah land surface model advances in the national centers for environmental prediction operational mesoscale eta model, *J. Geophys. Res.*, *108*(D22), 8851, doi:10.1029/2002JD003296.

Gerbig, C., S. Schmitgen, D. Kley, A. Volz-Thomas, K. Dewey, and D. Haaks (1999), An improved fast-response vacuum-UV resonance fluorescence CO instrument, *J. Geophys. Res.*, *104*(D1), 1699–1704, doi:10.1029/1998JD100031.

Homeyer, C. R. (2014), Formation of the enhanced-V infrared cloud-top feature from high-resolution three-dimensional radar observations, *J. Atmos. Sci.*, *71*(1), 332–348, doi:10.1175/JAS-D-13-079.1.

Homeyer, C. R., K. P. Bowman, and L. L. Pan (2010), Extratropical tropopause transition layer characteristics from high-resolution sounding data, *J. Geophys. Res.*, *115*(D13), doi:10.1029/2009JD013664.

Hong, S.-Y., Y. Noh, and J. Dudhia (2006), A new vertical diffusion package with an explicit treatment of entrainment processes, *Mon. Wea. Rev.*, *134*(9), 2318–2341, doi:10.1175/MWR3199.1.

Jaeglé, L. (2007), Pumping up surface air, *Science*, *315*(5813), 772–773, doi:10.1126/science.1138988.

Jaeglé, L., D. J. Jacob, P. O. Wennberg, C. M. Spivakovsky, T. F. Hanisco, E. J. Lanzendorf, E. J. Hintsa, D. W. Fahey, E. R. Keim, M. H. Proffitt, E. L. Atlas,

F. Flocke, S. Schauffler, C. T. McElroy, C. Midwinter, L. Pfister, and J. C. Wilson (1997), Observed OH and HO_2 in the upper troposphere suggest a major source from convective injection of peroxides, *Geophys. Res. Lett.*, *24*(24), 3181–3184, doi:10.1029/97GL03004.

Janjić, Z. I. (1994), The step-mountain eta coordinate model: Further developments of the convection, viscous sublayer, and turbulence closure schemes, *Mon. Wea. Rev.*, *122*(5), 927–945, doi:10.1175/1520-0493(1994)122⟨0927:TSMECM⟩2.0.CO;2.

Janjić, Z. I. (1996), The surface layer in the ncep eta model, in *Proceedings of the 11th Conference on Numerical Weather Prediction*, pp. 354–355, Am. Meteorol. Soc., Norfolk, VA.

Kosterev, A. A., F. K. Tittel, R. Köhler, C. Gmachl, F. Capasso, D. L. Sivco, A. Y. Cho, S. Wehe, and M. G. Allen (2002), Thermoelectrically cooled quantum-cascade-laser-based sensor for the continuous monitoring of ambient atmospheric carbon monoxide, *Appl. Opt.*, *41*(6), 1169–1173, doi:10.1364/AO.41.001169.

Lacis, A. A., D. J. Wuebbles, and J. A. Logan (1990), Radiative forcing of climate by changes in the vertical distribution of ozone, *J. Geophys. Res.*, *95*(D7), 9971–9981, doi:10.1029/JD095iD07p09971.

Lelieveld, J., and P. J. Crutzen (1994), Role of deep cloud convection in the ozone budget of the troposphere, *Science*, *264*(5166), 1759–1761, doi:10.1126/science.264.5166.1759.

Liu, S. C., D. Kley, M. McFarland, J. D. Mahlman, and H. Levy (1980), On the origin of tropospheric ozone, *J. Geophys. Res.*, *85*(C12), 7546–7552, doi:10.1029/JC085iC12p07546.

Logan, J. A. (1983), Nitrogen oxides in the troposphere: Global and regional budgets, *J. Geophys. Res.*, *88*(C15), 10,785–10,807, doi:10.1029/JC088iC15p10785.

Mlawer, E. J., S. J. Taubman, P. D. Brown, M. J. Iacono, and S. A. Clough (1997), Radiative transfer for inhomogeneous atmospheres: RRTM, a validated correlated-k model for the longwave, *J. Geophys. Res.*, *102*(D14), 16,663–16,682, doi:10.1029/97JD00237.

Orville, R. E. (2008), Development of the National Lightning Detection Network, *Bull. Amer. Meteor. Soc.*, *89*(2), 180–190, doi:10.1175/BAMS-89-2-180.

Pan, L. L., K. P. Bowman, E. Atlas, S. C. Wofsy, F. Zhang, J. F. Bresch, B. A. Ridley, J. V. Pittman, C. Homeyer, P. Romashkin, and W. A. Cooper (2010), The Stratosphere-Troposphere Analyses of Regional Transport 2008 (START08) Experiment, *Bull. Amer. Meteor. Soc.*, *91*(3), 327–342, doi: 10.1175/2009BAMS2865.1.

Pickering, K. E., A. M. Thompson, R. R. Dickerson, W. T. Luke, D. P. McNamara, J. P. Greenberg, and P. R. Zimmerman (1990), Model calculations of tropospheric ozone production potential following observed convective events, *J. Geophys. Res.*, *95*(D9), 14,049–14,062, doi:10.1029/JD095iD09p14049.

Poulida, O., R. R. Dickerson, and A. Heymsfield (1996), Stratosphere-troposphere exchange in a midlatitude mesoscale convective complex: 1. Observations, *J. Geophys. Res.*, *101*(D3), 6823–6836, doi:10.1029/95JD03523.

Proffitt, M. H., and R. J. McLaughlin (1983), Fast-response dual-beam UV-absorption ozone photometer suitable for use on stratospheric balloons, *Rev. Sci. Instrum.*, *54*(12), 1719–1728, doi:10.1063/1.1137316.

Ridley, B., E. Atlas, H. Selkirk, L. Pfister, D. Montzka, J. Walega, S. Donnelly, V. Stroud, E. Richard, K. Kelly, A. Tuck, T. Thompson, J. Reeves, D. Baumgardner, W. Rawlins, M. Mahoney, R. Herman, R. Friedl, F. Moore, E. Ray, and J. Elkins (2004a), Convective transport of reactive constituents to the tropical and mid-latitude tropopause region: I. observations, *Atmos. Environ.*, *38*(9), 1259–1274, doi:10.1016/j.atmosenv.2003.11.038.

Ridley, B., L. Ott, K. Pickering, L. Emmons, D. Montzka, A. Weinheimer, D. Knapp, F. Grahek, L. Li, G. Heymsfield, M. McGill, P. Kucera, M. J. Mahoney, D. Baumgardner, M. Schultz, and G. Brasseur (2004b), Florida thunderstorms: A faucet of reactive nitrogen to the upper troposphere, *J. Geophys. Res.*, *109*(D17), doi: 10.1029/2004JD004769.

Schumann, U., and H. Huntrieser (2007), The global lightning-induced nitrogen oxides source, *Atmos. Chem. Phys.*, *7*(14), 3823–3907, doi:10.5194/acp-7-3823-2007.

Seinfeld, J. H., and S. N. Pandis (2006), *Atmospheric Chemistry and Physics: From Air Pollution to Climate Change*, 2^{nd} ed., 1203 pp., John Wiley & Sons, Inc., Hoboken, New Jersey.

Skamarock, W. C., J. G. Powers, M. Barth, J. E. Dye, T. Matejka, D. Bartels, K. Baumann, J. Stith, D. D. Parrish, and G. Hubler (2000), Numerical simulations of the July 10 Stratospheric-Tropospheric Experiment: Radiation, Aerosols, and Ozone/Deep Convection Experiment convective system: Kinematics and transport, *J. Geophys. Res.*, *105*(D15), 19,973–19,990, doi:10.1029/2000JD900179.

Stenchikov, G., R. Dickerson, K. Pickering, W. Ellis, B. Doddridge, S. Kondragunta, O. Poulida, J. Scala, and W.-K. Tao (1996), Stratosphere-troposphere exchange in

a midlatitude mesoscale convective complex: 2. Numerical simulations, *J. Geophys. Res.*, *101*(D3), 6837–6851, doi:10.1029/95JD02468.

Tao, W.-K., J. Simpson, and M. McCumber (1989), An ice-water saturation adjustment, *Mon. Wea. Rev.*, *117*(1), 231–235, doi:10.1175/1520-0493(1989)117⟨0231:AIWSA⟩2.0.CO;2.

World Meteorological Organization (1957), Meteorology—a threedimensional science: Second session of the commission for aerology, *World Metetrol. Organ. Bull.*, *4*, 134–138.

Zondlo, M. A., M. E. Paige, S. M. Massick, and J. A. Silver (2010), Vertical cavity laser hygrometer for the National Science Foundation Gulfstream-V aircraft, *J. Geophys. Res.*, *115*(D20), doi:10.1029/2010JD014445.